JOURNAL OF GEOPHYSICAL RESEARCH, VOL. 108, NO. A10, 1377, doi:10.1029/2002JA009776, 2003

Are coronal holes the only source of fast solar wind at solar minimum?

Y. Q. Hu[1,2] and S. R. Habbal[1]
Institute of Mathematical and Physical Sciences, University of Wales, Aberystwyth, UK

Y. Chen[2]
Harvard-Smithsonian Center for Astrophysics, Cambridge, Massachusetts, USA

X. Li
Institute of Mathematical and Physical Sciences, University of Wales, Aberystwyth, UK

Received 11 November 2002; revised 17 July 2003; accepted 23 July 2003; published 28 October 2003.

[1] A two-dimensional (2-D) MHD model of an Alfvén-wave-driven solar wind in the heliospheric meridional plane is presented whereby the consequences of a magnetic field distribution at the Sun that digresses from the standard dipole structure, often used in 2-D MHD models, are explored. The latitudinal distribution of open magnetic flux is specified at the solar surface, with a clear distinction between the polar coronal hole and the neighboring quiet Sun. The region of strictly closed magnetic structures at the coronal base is limited in latitude to ±30°. Alfvén waves are assumed to emanate from the solar surface above 30° latitude so as to open the field lines anchored there, as well as heat and accelerate the solar wind. The field lines anchored at the solar surface below 30° latitude, where the plasma is thermally conductive, remain closed, resulting in the formation of the helmet streamer astride the solar equator. The solution obtained is characterized by a helmet streamer in magnetostatic equilibrium, centered at the solar equator, and a steady solar wind outside. With the assumption that the contribution of the polar coronal hole and the quiet Sun to the interplanetary magnetic flux is evenly split between them during solar minimum, a fast wind solution is obtained that matches the latitudinal distribution of the solar wind parameters observed by Ulysses and SOHO and extends from the pole to 9° latitude. The larger fraction (≈60%) of the fast wind (above 30° latitude at 1 AU) emerges from the polar coronal hole, while the remainder is associated with the quiet Sun. While the actual fraction of the fast solar wind originating from polar coronal holes relies on an accurate estimate of the contribution of the open magnetic flux from polar coronal holes to the total IMF flux, this model shows that extending the source of open magnetic flux at the Sun beyond the traditionally assumed polar coronal holes can readily account for the latitudinal distribution of fast wind measured by Ulysses at solar minimum. *INDEX TERMS:* 2169 Interplanetary Physics: Sources of the solar wind; 7843 Space Plasma Physics: Numerical simulation studies; 2164 Interplanetary Physics: Solar wind plasma; 2159 Interplanetary Physics: Plasma waves and turbulence; *KEYWORDS:* coronal holes, fast solar wind, 2-D MHD solar wind model, Alfvén wave driven solar wind

Citation: Hu, Y. Q., S. R. Habbal, Y. Chen, and X. Li, Are coronal holes the only source of fast solar wind at solar minimum?, *J. Geophys. Res.*, *108*(A10), 1377, doi:10.1029/2002JA009776, 2003.

1. Introduction

[2] The concept of coronal holes as the source of the fast wind was first proposed by *Krieger et al.* [1973] and has since been widely accepted. On the other hand, the impression of the outer corona from white light measurements led to the idea that open field lines existed solely in coronal holes [*Zirker*, 1977] and to the conclusion that the fast wind observed by Ulysses all came from polar coronal holes [*Gosling et al.*, 1995; *Geiss et al.*, 1995; *McComas et al.*, 1998]. Whether coronal holes are the sole source of the fast wind, however, is not without question. *Burlaga et al.* [1978] found that some of the magnetic fields and high-speed streams observed at 1 AU were related to open field regions on the Sun which were not associated with known coronal holes and suggested that open field lines may be more basic than coronal holes as sources of the solar wind. *Zhao and Hoeksema* [1995] used the Wilcox Solar Observatory photospheric magnetic field observations to

[1]Also at Harvard-Smithsonian Center for Astrophysics, Cambridge, Massachusetts, USA.
[2]Also at School of Earth and Space Sciences, University of Science and Technology of China, Hefei, China.

0148-0227/03/2002JA009776$09.00

account for the interplanetary magnetic field (IMF) and found that if some interplanetary flux originates outside coronal holes, their model can match the observed IMF using the accepted saturation factor of 1.8 for λ5250 magnetograph observations. If the open flux is required to come exclusively from coronal holes, then an additional factor of two is needed. The same additional factor was used by *Wang and Sheeley* [1988] in the treatment of the WSO photospheric field measurements in order to match their model prediction with IMF observations. The enhanced correction factor is based on a careful comparison of measurements made in λ5250 and λ5233 by *Ulrich* [1992] and discussed in detail by *Wang and Sheeley* [1995, 2002]. *Svalgaard et al.* [1978] found that the magnetic flux density peaks at 1.15 mT at the pole and decreases to 0.2 mT at the polar cap boundary of 55° latitude and that the total open flux through either polar cap is about 3×10^{14} Wb. This flux amounts to about 60% of the total IMF flux, if the average radial field at 1 AU is taken to be 3.5 nT [cf. *Smith and Balogh*, 1995]. Consequently, one might conjecture that about one-half of the IMF flux comes from open field regions on the solar surface outside polar coronal holes. If this conjecture is correct, then one-half of the solar wind in the heliosphere should be associated with these regions.

[3] The fast wind observed by Ulysses during solar minimum filled about 63% of the heliosphere [*Gosling et al.*, 1995]. Based on the above-mentioned conjecture, at least 13% of the fast solar wind emerges from the open field regions outside polar coronal holes. The actual percentage of the fast wind in the heliosphere might be even larger in view of the fact that the heliospheric current sheet and the associated slow wind belt are tilted and warped relative to the solar equator so that the latitudinal width of the slow wind belt might be overestimated in the Ulysses observations. Indeed, a series of narrow streams of fast wind were actually observed in the slow wind belt. Therefore not only the entire slow wind but also a remarkable part of the fast wind must emerge from open field regions outside polar coronal holes. Based on radio, ultraviolet, white-light, and in situ plasma measurements, Woo and Habbal found evidences in support of the view that the fast wind emerges from both polar coronal holes and the quiet Sun, i.e., the solar surface other than coronal holes and active regions [*Woo and Habbal*, 1997, 1999a, 1999b; *Habbal et al.*, 1997; *Woo et al.*, 1999]. We will use the term ''quiet Sun'' hereinafter to refer specifically to open field regions outside polar coronal holes, and excluding active regions. *Habbal and Woo* [2001] made a quantitative comparison of the latitudinal profile of the polarized brightness (pB) measurements at 1.15 R_s (R_s is the solar radius) and Ulysses interplanetary measurements of the fast wind during its first south polar passage and concluded that the fast wind observed by Ulysses should originate from both regions. While viewed from different perspectives, these works came to the same conclusion that part of the fast solar wind might originate from the quiet Sun.

[4] A number of two-dimensional (2-D) MHD numerical simulations have been recently carried out to reproduce the latitudinal profiles of the solar wind plasma properties measured by Ulysses during the polar passes at solar minimum [e.g., *Suess et al.*, 1999; *Usmanov et al.*, 2000; *Chen and Hu*, 2001]. With the same constraint at 1 AU set by Ulysses observations and 2-D approximation, the simulations to be presented here differ from previous ones in the following two aspects. First, as mentioned above, we intend to explore the possibility theoretically that at solar minimum, the fast solar wind can originate from both the polar coronal holes and the quiet Sun. The associated assumption is that the polar coronal hole contributes only half of the IMF flux, whereas the other half comes from the quiet Sun. While the magnetic field is open both in the polar coronal hole and in the quiet Sun, a major difference lies in that the quiet Sun has a higher density, which distinguishes it from the polar coronal hole in terms of white light measurements. It will be shown that a fast solar wind may emerge from the quiet Sun much the same despite a higher density at the base. Second, Alfvén waves are taken to be the only external source for the heating and acceleration of the solar wind. By ''external,'' we here mean that the waves emanate from the solar surface as a boundary condition and transfer energy and momentum to the solar wind plasma unidirectionally. While this is a highly idealized assumption on the energetics of the solar wind, it provides us the opportunity to accurately control the energy deposition in the region above the solar surface. This is crucial if a steady solar wind solution is sought. For instance, if a volumetric heating is used in terms of a given function of space, it would be very difficult to prevent the streamer from being heated, since one cannot even predict the boundary of the streamer a priori. As pointed out by *Suess et al.* [1996], the addition of a volumetric source to the streamer causes a slow, continuing expansion and stripping of magnetic flux from the top of the streamer until the streamer essentially evaporates and the field is fully open to the interplanetary medium. They also found that thermal conduction does not quench the evaporation. In the case when the volumetric heating in the streamer is sufficiently small so that the energy addition happens to be compensated by a continuous or intermittent energy release from the top of the streamer, the resultant numerical solution would become truly time-dependent and can never converge to a truly steady state. Using a purely polytropic model with a polytropic index of 1.05 without introducing additional volumetric heating, *Washimi et al.* [1987] created a 2-D solar wind solution. Starting from a dipole field, they obtained a new magnetic configuration that was typical for 2-D solar wind solutions. However, they noted that the boundary between the open and closed field regions was not clear at the equator, and the solution was not an exact steady state. Now let us return to our model. Since Alfvén waves propagate strictly along the field lines, it becomes easy to control the boundary between the open and closed field regions and to prevent exotic energy deposition in the streamer. As a matter of fact, we may divide the solar surface into ''open'' and ''closed'' field regions a priori and then introduce Alfvén waves only in the ''open'' field region. Under the action of these waves, all field lines anchored in the ''open'' region will eventually become open to the interplanetary medium irrespective as to whether they are closed or open initially. As far as the ''closed'' region is concerned, the field lines may be a mixture of open and closed ones determined by the solution. However, for a moderate magnetic flux which is set equal to that in the ''open'' region and has a relatively narrow latitudinal span (60° in total), the tension of the magnetic

field happens to be capable of confining the hot plasma in quasi-equilibrium and the magnetic field obtained thus becomes completely closed (see section 2.3 for details). As such, a quasi-steady state is achieved in accord with the appointed open and closed regions at the solar surface, and no energy input is applied to the streamer. Moreover, the observed extension of polar coronal holes near solar minimum is typically 30° from the pole. Therefore in order to demonstrate that part of the fast wind may emerge from outside the polar coronal hole, we simply assume that the border of the "open" field region lies at 30° latitude, and the interface between the polar coronal hole and the quiet Sun lies at 60° latitude. Then the goal of this study is to show that the plasma flow launched from the region between 30° and 60° latitude may produce a fast wind at 1 AU like that from the polar coronal hole.

[5] The plan of the paper is as follows. The governing equations and initial-boundary conditions are described in section 2. The numerical techniques developed to improve the accuracy of mass and energy conservation and to guarantee the convergence of the numerical solution to a steady state are given in section 3. The numerical results are discussed in section 4. Concluding remarks are given in section 5.

2. Numerical Model and Initial-Boundary Conditions

2.1. Governing Equations

[6] For axisymmetrical MHD flows in spherical coordinates (r, θ, φ), a magnetic flux function ψ (t, r, θ) is introduced and is related to the magnetic field by

$$\mathbf{B} = \nabla\psi \times \frac{\hat{\varphi}}{r\sin\theta}. \tag{1}$$

We assume that the solar wind is driven by Alfvén waves that propagate away from the Sun along open field lines. The two-dimensional, two-component MHD equations in the meridional plane with Alfvén waves may therefore be cast into the following form:

$$\frac{\partial \rho}{\partial t} + \nabla\cdot(\rho\mathbf{v}) = 0, \tag{2}$$

$$\frac{\partial \mathbf{v}}{\partial t} + \mathbf{v}\cdot\nabla\mathbf{v} + \frac{1}{\rho}\nabla\left(p_e + p_p + p_w\right) + \frac{1}{\mu_0\rho}L\psi\nabla\psi + \frac{GM_s}{r^2}\hat{\mathbf{r}} = 0, \tag{3}$$

$$\frac{\partial \psi}{\partial t} + \mathbf{v}\cdot\nabla\psi = 0, \tag{4}$$

$$\frac{\partial T_e}{\partial t} + \mathbf{v}\cdot\nabla T_e + (\gamma-1)T_e\nabla\cdot\mathbf{v} + \nu_E\left(T_e - T_p\right) - \frac{\gamma-1}{\rho R}\nabla\cdot(\mathbf{K}_e\cdot\nabla T_e) = 0, \tag{5}$$

$$\frac{\partial T_p}{\partial t} + \mathbf{v}\cdot\nabla T_p + (\gamma-1)T_p\nabla\cdot\mathbf{v} + \nu_E\left(T_p - T_e\right) - \frac{\gamma-1}{\rho R}Q = 0, \tag{6}$$

$$\frac{\partial p_w}{\partial t} + \nabla\cdot\left[\left(\frac{3}{2}\mathbf{v} + \mathbf{v}_A\right)p_w\right] - \frac{\mathbf{v}}{2}\cdot\nabla p_w + \frac{Q}{2} = 0, \tag{7}$$

where

$$L\psi = \frac{1}{r^2\sin^2\theta}\left(\frac{\partial^2\psi}{\partial r^2} + \frac{1}{r^2}\frac{\partial^2\psi}{\partial\theta^2} - \frac{\cot\theta}{r^2}\frac{\partial\psi}{\partial\theta}\right),$$

ρ ($= nm_p$) is the plasma density, $\mathbf{v}$ is the flow velocity, T_e and T_p are the electron and proton temperature, $p_e = \rho R T_e$ and $p_p = \rho R T_p$ are the electron and proton pressure, $p_w = \rho\,\langle\delta v^2\rangle/2$ is the Alfvén wave pressure, G, M_s, R, μ_0 and γ are the gravitational constant, the mass of the Sun, the gas constant, the vacuum magnetic permeability, and the adiabatic index ($\gamma = 5/3$), respectively, and $\nu_E = \nu_{E0} n T_e^{-3/2}$ ($\nu_{E0} = 9.094 \times 10^{-8}$ $\mathrm{m^3K^{3/2}s^{-1}}$) is the electron-proton collision frequency [*Braginskii*, 1965]. A classical thermal conductivity that is only along the magnetic field is used for electrons [*Spitzer*, 1962]:

$$\mathbf{K}_e = \kappa_0 T_e^{5/2}\mathbf{BB}/B^2, \tag{8}$$

with $\kappa_0 = 0.78 \times 10^{-11}$ $\mathrm{J\cdot K^{-7/2}\cdot m^{-1}\cdot s^{-1}}$, whereas the proton thermal conduction has been ignored. Finally, Q is the wave dissipation rate and its expression will be given in section 2.2.3.

2.2. Boundary Conditions

[7] To save computational time, we separate the computational domain of (1–215 R_s) into two overlapping subdomains, (1–12 R_s) and (10–215 R_s). A 57 × 60 mesh is laid out for the inner subdomain, and a 100 × 60 mesh is laid for the outer one. The grid spacing in the r-direction increases in terms of a geometric series from 0.02 R_s at the coronal base to 0.62 R_s at 10 R_s, and 0.71 R_s at 12 R_s with a common ratio 1.067 for the inner subdomain, and from 0.62 R_s at 10 R_s to 4.88 R_s at 1 AU with a common ratio 1.021 for the outer subdomain. The mesh in the θ direction is the same for the two subdomains, being uniform between 60° and 90° with $\Delta\theta = 1°$ and increasing in terms of a geometric series from 1° at 60° to about 4° at the pole with a common ratio 1.051.

[8] For the outer subdomain the lower boundary is situated in the supersonic flow region, and all quantities are determined by the solution in the inner subdomain. As for the polar axis, and the equator, boundary conditions are the same for the two subdomains. In what follows, we only discuss the inner subdomain with its lower boundary at the coronal base. In order to obtain a consistent transonic solar wind solution, one can only specify five among the seven unknowns at the coronal base for the present case and should leave the other two free to change during the time evolution. The two free quantities are v_r and v_θ, which are determined by equivalent extrapolation of mass flux along flow tubes and the condition that $\mathbf{v} \parallel \mathbf{B}$. At the top, all quantities are evaluated by linear extrapolation except ρ, T_e and p_w. ρ is evaluated by equivalent extrapolation of mass flux along the radial direction, whereas T_e and p_w are extrapolated in terms of $r^{-2/7}$ and $r^{-3.5}$, respectively. The former means a vanishing electron thermal conductive flux, and the latter is based on the approximation that the Alfvén wave pressure decreases with r according to $r^{-3.5}$ at large

heliocentric distances. Symmetrical boundary conditions are used for the equator and polar axis. The specification of the other five unknowns at the coronal base is subject to available observational constraints and will be discussed in detail below.

2.2.1. Magnetic Flux Distribution

[9] Let us first discuss the distribution of the magnetic flux at the coronal base. In previous models, a dipole field was often taken as the initial background field for 2-D simulations in the heliospheric meridional plane; it had a specific distribution of the radial magnetic field on the solar surface that is proportional to cos θ. However, the magnetic flux distribution on the solar surface cannot be properly represented by a single dipole field. Near solar minimum, observations yield the following:

[10] 1. Within the polar coronal hole, the radial magnetic field is the strongest at the pole, and decreases with colatitude according to [*Svalgaard et al.*, 1978]

$$B_r = B_p \cos^8 \theta, \tag{9}$$

where B_p is of the order of 10 G.

[11] 2. The total closed flux equals 1–2 times the open flux at sunspot minimum [*Wang et al.*, 2000].

[12] 3. The magnetic flux emerging from polar coronal holes may probably constitute only about one half of the total interplanetary flux [*Zhao and Hoeksema*, 1995]. Therefore there must exist other open field regions outside polar coronal holes, which are responsible for the other half of the interplanetary flux.

[13] 4. From coronal images during solar eclipses one can clearly see that the half-width of helmet streamers is 30° at most.

[14] 5. The average radial magnetic field at 1 AU ranges from 3 to 3.5 nT [*Smith and Balogh*, 1995]. So the total interplanetary flux is $4–5 \times 10^{14}$ Wb, and should equal the total flux emerging from open field regions at the Sun.

[15] Based on the observations mentioned above, we divide the solar surface into three regions: the polar coronal hole, the quiet Sun, and the helmet streamer. In the numerical box ($0° \le \theta \le 90°$), the three regions are taken to be (0°, 30°), (30°, 60°), and (60°, 90°), respectively. The magnetic field is open in the polar coronal hole and the quiet Sun but closed in the streamer. The open flux is assumed to be equal to the closed flux, and the same amount of flux emerges from the polar coronal hole and the quiet Sun. The radial magnetic field is given by equation (9) in the coronal hole, is uniform in the quiet Sun, and varies with θ like a dipole field in the streamer. Consequently, the radial magnetic field on the solar surface is given by

$$B_r(1,\theta) = \begin{cases} B_p \cos^8 \theta, & 0° \le \theta < 30°, \\ B_q, & 30° \le \theta < 60°, \\ B_s \cos\theta, & 60° \le \theta \le 90°, \end{cases} \tag{10}$$

where B_p, B_q, and B_s are constants, determined by the given magnetic fluxes in the three regions. Assuming that the total interplanetary flux is $2\pi\psi_c$, then the magnetic flux is $\pi\psi_c$ for the coronal hole, $\pi\psi_c$ for the quiet Sun, and $2\pi\psi_c$ for the streamer. From this condition, we can determine the values of B_p, B_q and B_s, and the results are

$$B_p = \frac{9\psi_c}{2\left[1-\left(\sqrt{3}/2\right)^9\right]R_s^2} = \frac{6.199\psi_c}{R_s^2},$$

$$B_q = \frac{\psi_c}{(\sqrt{3}-1)R_s^2} = \frac{1.366\psi_c}{R_s^2}, \quad B_s = \frac{8\psi_c}{R_s^2}.$$

For $B_{rE} = 3.3$ nT, we have $\psi_c = 7.4 \times 10^{13}$ Wb, $B_p = 9.46$ G, $B_q = 2.08$ G, and $B_s = 12.2$ G. Then the radial field at the streamer border (θ = 60°) is 6.1 G. The corresponding magnetic flux function on the solar surface is

$$\psi_0 = \begin{cases} \dfrac{1-\cos^9\theta}{2\left[1-\left(\sqrt{3}/2\right)^9\right]}\psi_c, & 0° \le \theta < 30°, \\ \dfrac{\sqrt{3}-\cos\theta-0.5}{\sqrt{3}-1}\psi_c, & 30° \le \theta < 60°, \\ 2\left(2\sin^2\theta-1\right)\psi_c, & 60° \le \theta \le 90°. \end{cases} \tag{11}$$

Notice that $\psi_0(0°) = 0$, $\psi_0(30°) = \psi_c/2$, $\psi_0(60°) = \psi_c$, and $\psi_0(90°) = 2\psi_c$ are consistent with our specification of the magnetic flux distribution on the solar surface. The radial field and magnetic flux on the solar surface specified above are shown in Figure 1a by solid and dashed curves, respectively. For comparison, we also show the profile of the total magnetic field strength, B_0, at the solar surface as a dotted curve in Figure 1a for the steady state solution obtained for case A (see below).

2.2.2. Thermodynamic Conditions

[16] Near the solar surface ($r = 1.15\ R_s$) in the helmet streamer, the temperature is in the range of $1.7–2.1 \times 10^6$ K and the electron density $0.68–2.24 \times 10^8$ cm^3 [*Li et al.*, 1998]. The electron density at $r = 1.15\ R_s$ outside the streamer increases from the pole to the streamer by a factor of 2 [*Habbal and Woo*, 2001]. Based on these observations, we specify the temperature and density profiles at the coronal base as follows:

$$T_{e0} = T_{p0} = \begin{cases} 10^6 \text{ K}, & 0° \le \theta < 60°, \\ 2 \times 10^6 \text{ K}, & 60° \le \theta \le 90°, \end{cases} \tag{12}$$

$$\rho_0 = \begin{cases} 2.505 \times 10^{-16} (\cos\theta)^{-1} \text{ g} \cdot \text{cm}^{-3}, & 0° \le \theta < 60°, \\ 5.01 \times 10^{-16} \text{ g} \cdot \text{cm}^{-3}, & 60° \le \theta \le 90°. \end{cases} \tag{13}$$

The corresponding number density is 1.5×10^8 cm^{-3} at the pole and 3×10^8 cm^{-3} at the equator. The gas pressure is 4.14×10^{-2} dyn·cm^{-2} at the pole, and the corresponding plasma β, i.e., the ratio of gas pressure to magnetic pressure, is about 0.012. The temperature and density distributions given at the coronal base are shown in Figure 1b. Note that the density in the quiet Sun is higher than that in the polar coronal hole as implied by white light measurements.

2.2.3. Alfvén Wave Energy Flux

[17] Alfvén waves have been considered as an efficient mechanism for heating and accelerating the fast solar wind in a number of 1-D solar wind models [*Hollweg*, 1986;

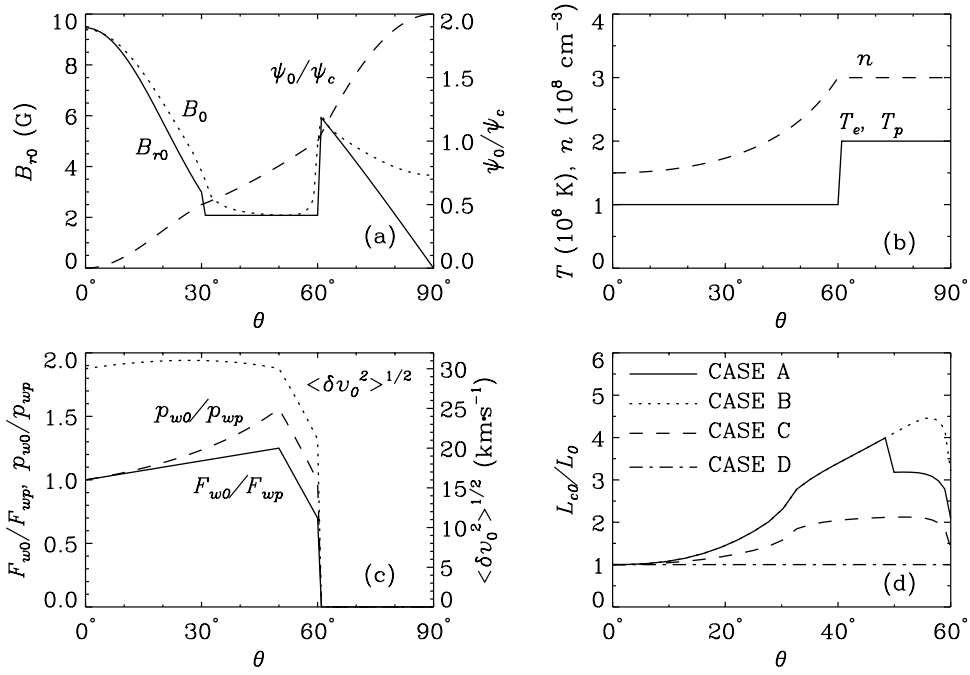

Figure 1. Boundary conditions at the coronal base for (a) magnetic field and flux function, (b) temperature and density, (c) wave pressure, energy flux, and amplitude, and (d) dissipation length for the four cases considered. The coronal base is divided into three regions: the polar coronal hole ($0° \leq \theta < 30°$), the quiet Sun ($30° \leq \theta < 60°$), and the helmet streamer ($60° \leq \theta \leq 90°$).

Hollweg and Johnson, 1988; *Tu*, 1987; *Hu et al.*, 1997; *Tu and Marsch*, 1997; *Marsch and Tu*, 1997; *Li et al.*, 1999; *Hu et al.*, 1999] and recently, in 2-D solar wind models [*Usmanov et al.*, 2000; *Chen and Hu*, 2001]. The cascade and dissipation of Alfvén waves depends on the wave spectrum. A rigorous approach is to simultaneously solve the equations for the wave spectrum and the solar wind flow [*Tu*, 1987; *Hu et al.*, 1999]. In order to avoid the complexity associated with the solution of the wave spectrum equation, we follow the approach proposed by *Hollweg* [1986], namely, we start from the wave pressure equation (7) with a prescribed dissipation rate Q. For the reason mentioned by *Chen and Hu* [2001], we take the Kolmogorov rate proposed by *Hollweg* [1986]:

$$Q_{\rm kol} = \frac{\rho\langle\delta v^2\rangle^{3/2}}{L_c} = \frac{2\sqrt{2}p_w^{3/2}}{\sqrt{\rho}L_c}, \tag{14}$$

where $\langle\delta v^2\rangle$ is the velocity variance associated with the wave field and L_c the correlation length of the fluctuations.

[18] For 1-D wave-driven solar wind simulations, both the wave amplitude and the dissipation length on the solar surface are important parameters. The former determines the total energy flux provided by Alfvén waves, (after being normalized to 1 AU [*Hu et al.*, 1997])

$$F_{w0} = \sqrt{\frac{\rho_0}{\mu_0}}B_{rE}\langle\delta v_0^2\rangle = \frac{2B_{rE}p_{w0}}{\sqrt{\mu_0\rho_0}}, \tag{15}$$

where ρ_0, $\langle\delta {v_0}^2\rangle^{1/2}$, and $p_{w0} = \rho_0\,\langle\delta {v_0}^2\rangle/2$ are the density, the wave amplitude (i.e., the square root of the wave velocity variance), and the wave pressure at the coronal base, respectively, and B_{rE} is the radial component of the magnetic field at 1 AU. Note that F_{w0} does not depend on the field strength at the coronal base. This is because with the density and wave pressure given at the base, an increase of the field strength there results in an increased expansion of the related flow tube so that the resulting energy flux normalized to 1 AU remains unchanged and depends on B_{rE} instead. As seen from equation (15), F_{w0} is proportional to ${p_{w0}/\rho_0}^{1/2}$. Based on Ulysses measurements at solar minimum [see *McComas et al.*, 2000], we can calculate the energy flux of the solar wind at 1 AU that is approximately equal to the sum of the kinetic and gravitational potential energy fluxes, as a function of θ. The energy flux carried by protons and alpha particles increases slightly with colatitude in the fast wind region from 1.7 ergs·cm^{-2}·s^{-1} at the pole to 2.0 ergs·cm^{-2}·s^{-1} at $\theta = 54°$. The slow wind has a lower energy flux than that of the fast wind, about 70% of that at the pole. Our model does not include alpha particles, so the figures mentioned above should be reduced by about 20%. On this basis, we assume a wave amplitude of 30 km·s^{-1} at the pole, hence a wave pressure of $p_{wp} = 1.127 \times 10^{-3}$ dyn·cm^{-2} and a wave energy flux $F_{wp} = 1.326$ ergs·cm^{-2}·s^{-1}. The wave energy flux is further assumed to increase linearly with θ from F_{wp} at the pole to $1.25F_{wp}$ at $\theta = 50°$ and then drops linearly with θ to $0.7F_{wp}$ at the border of the streamer ($\theta = 60°$). At the base of the streamer we take $F_{w0} = 0$, to inhibit wave energy addition to the streamer so that the field lines there remain closed. Therefore the wave energy flux at the coronal base is expressed as

$$F_{w0} = \begin{cases} F_{wp}[1 + 0.02\theta(f_2 - 1)], & 0° \leq \theta < 50°, \\ F_{wp}[f_1 + 0.1(f_2 - f_1)(60° - \theta)], & 50° \leq \theta < 60°, \\ 0, & 60° \leq \theta \leq 90°, \end{cases} \tag{16}$$

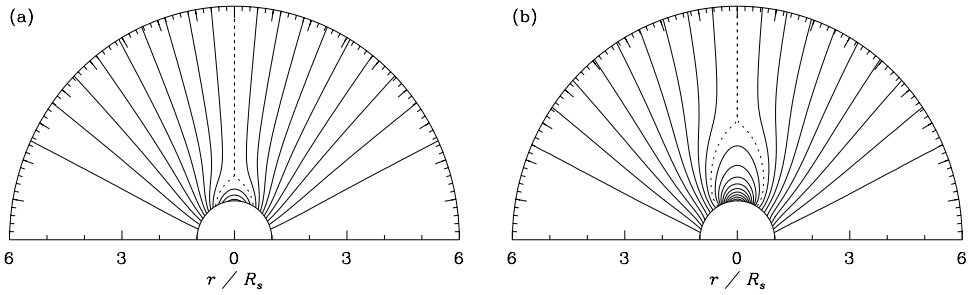

Figure 2. Magnetic field configuration for (a) the initial guess, and (b) the steady state solution of case A. The dotted curve depicts the equatorial current sheet and the streamer border with $\psi = \psi_c$. The field lines are equally spaced by 0.1 ψ_c. The cusp point is located at a heliocentric distance of 1.62 R_s for the initial guess and stabilizes at 3.0 R_s for the steady state.

where $f_1 = 0.7$ and $f_2 = 1.25$. The colatitudinal profile of F_{w0} is given by the solid curve in Figure 1c. The wave pressure at the coronal base can be evaluated from $p_{w0} = p_{wp}F_{w0}\sqrt{\rho_0}/(F_{wp}\sqrt{\rho_p})$, where ρ_p is the density at the pole. It increases from p_{wp} at the pole to 1.56 p_{wp} at $\theta = 50°$, and then decreases to 0.99 p_{wp} at $\theta = 60°$ (i.e., the edge of the open field region), as shown by the dashed curve in Figure 1c. The wave amplitude $\langle \delta v_0^2 \rangle^{1/2}$, however, has its maximum of 31.1 km·s^{-1} at 27° instead of 50° and then decreases monotonically to 21.1 km·s^{-1} at $\theta = 60°$, as shown by the dotted line in Figure 1c.

2.2.4. Alfvén Wave Dissipation Length

[19] The wave dissipation length along a given flow tube is expressed by [*Hollweg*, 1986]

$$L_c = L_{c0}(B_0/B)^{1/2}, \tag{17}$$

where L_{c0} and B_0 are the dissipation length and the magnetic field strength at the base of the flow tube respectively. For the present 2-D case, both L_{c0} and B_0 may be different for different flow tubes, namely, they may depend on ψ that labels the flow tubes. In fact, B_0 is consistently determined by the solar wind solution. Therefore one can only adjust L_{c0} on the solar surface to control the properties of the 2-D solar wind solutions. We have tried various choices of L_{c0} and will show the steady state solutions for four typical cases, labeled cases A, B, C, and D, respectively. Among these cases, case A is the closest to match Ulysses measurements. We will mainly discuss this case for which

$$L_{c0} = \begin{cases} \sqrt{B_p/B_0}\left[1 + 1.3(\psi_0/\psi_c)^{\frac{3}{2}}\right]L_0, & 0 \le \psi_0/\psi_c < 0.8, \\ 1.5\sqrt{B_p/B_0}L_0, & 0.8 \le \psi_0/\psi_c \le 1. \end{cases} \tag{18}$$

All numbers in equation (18) were determined by a trial-and-error procedure, including L_0, that is the dissipation length at the pole, taken to be 4×10^4 km. With B_0 obtained in the related steady state solution (see Figure 1a), the colatitudinal profile of L_{c0} is shown in Figure 1d as a solid line as a function of θ. If the first expression in equation (18), originally limited to the region of 0–0.8 ψ_c, is extended to the whole open field region (0–1 ψ_c), then we get case B, for which L_{c0} is shown as a dotted line in Figure 1d. In the work by *Chen and Hu* [2001], L_{c0} was chosen to be $L_{c0} = L_0(B_p/B_0)^{1/2}$ so that $L_c = L_0(B_p/B)^{1/2}$. We refer to this case as case C. The fourth choice is to take L_{c0} to be constant, i.e., $L_{c0} = L_0$, referred to as case D. The profiles of L_{c0} are also shown in Figure 1d for the latter two cases. We will find soon that the solutions in the latter three cases fail to match Ulysses observations.

2.3. Initial Conditions

[20] In order for the magnetic field to have the prescribed magnetic flux distribution, we first take a partly open field as the initial field with the open flux exactly equal to $2\pi\psi_c$ and the border between the closed and open fields exactly rooted at $\theta = 60°$. To this end, let us start with the solution derived by *Low* [1986]:

$$\psi_a(r,\theta) = r(1-v^2)\left[(1+u^2)\arctan\left(\frac{1}{u}\right) - u\right] - \frac{\pi a^2 \sin^2\theta}{2r} + 2a\eta, \tag{19}$$

where

$$u^2 = \frac{1}{2}\left[\left(1-\frac{a^2}{r^2}\right)^2 + \frac{4a^2}{r^2}\cos^2\theta\right]^{1/2} - \frac{1}{2}\left(1-\frac{a^2}{r^2}\right),$$

$$v^2 = \frac{1}{2}\left[\left(1-\frac{a^2}{r^2}\right)^2 + \frac{4a^2}{r^2}\cos^2\theta\right]^{1/2} - \frac{1}{2}\left(1-\frac{a^2}{r^2}\right),$$

$$\eta^2 = \frac{1}{2}\left[\left(1-\frac{r^2}{a^2}\right)^2 + \frac{4r^2}{a^2}\cos^2\theta\right]^{1/2} - \frac{1}{2}\left(1-\frac{r^2}{a^2}\right).$$

Notice that $(r, \theta) = (a, 90°)$ is the neutral point, at which the field strength associated with ψ_a vanishes. The initial magnetic flux function that we need is simply expressed by

$$\psi(0,r,\theta) = \frac{\psi_a(r,\theta) - \psi_a(R_s,0)}{\psi_a(a,90°) - \psi_a(R_s,0)}\psi_c, \tag{20}$$

of which the total open flux is exactly the required value of $2\pi\psi_c$, regardless of a. To set the border of the closed and open fields at $\theta = 60°$ on the solar surface, we may evaluate $\psi(0, R_s, \theta)$ from equation (20) and then find θ_c at which $\psi(0, R_s, \theta_c) = \psi_c$. θ_c will decrease with decreasing a, so we may determine the value of a through iteration at which $\theta_c = 60°$. The required value of a is found to be 1.62. Then the initial magnetic field is determined from equations (19) and (20) with $a = 1.62$, and its configuration is shown in Figure 2a,

where the contour levels are integral times of 0.1 ψ_c, and the dotted curve ($\psi = \psi_c$) represents the equatorial current sheet and the border of the closed field, which intersect at the neutral point. While the initial field obtained has the required total open flux and colatitude of the border between the closed and open fields, its flux distribution on the solar surface, $\psi(0, R_s, \theta)$, is different from equation (11). In particular, the closed flux per radian is 0.34 ψ_c instead of the required ψ_c, whereas the open flux per radian from the coronal hole region ($\theta \leq 30°$) is only $\psi_c/3$ instead of the required $\psi_c/2$. This does not matter, however, because we can change the boundary value of ψ at the beginning of the time-dependent simulation, until the magnetic flux distribution equation (11) is achieved. The change is finished in the first 10 hours in physical time of the simulation that lasts 300 hours, and the magnetic flux function is fixed on the solar surface later on during the simulation. This change involves a magnetic flux emergence, 0.66 ψ_c per radian, into the streamer, and a shift of flux, $\psi_c/6$ per radian, from the quiet sun to the coronal hole. As a result, the final steady state solution obtained has the right magnetic flux distribution on the solar surface as required by equation (11).

[21] Given the magnetic flux distribution at the solar surface, the ratio of open to closed flux should be determined by the magnetohydrodynamics of the solar wind flow. In our case, this ratio is approximately determined by the ratio between the flux below 30° latitude to that above. This implies that the field lines anchored below 30° are completely closed since those anchored above 30° are presumably forced to open by the Alfvén waves. Therefore we need only explain why these field lines are closed instead of being partly open. In general, there exist two processes which control the openness of the field lines near by the streamer border. First, the ratio of plasma pressure to magnetic pressure, β, is much larger than unity at the top of the streamer, so the plasma there is apt to be pulled out of the streamer against the tension of the magnetic field, causing the corresponding closed field lines to open. This was considered by *Washimi et al.* [1987] as the main reason why a steady state was not obtained. Second, magnetic reconnection takes place across the equatorial current sheet, leading to the closing of the field lines right next to the sheet. The balance between the two competing effects depends on two factors. One is associated with the energetics both in the streamer and in the solar wind; different energy deposition in the corona yield different solar wind models. In our model, Alfvén waves are taken to be the only external energy source, and in addition, the wave energy flux is set to be zero below 30° latitude (see equation (16)). As a result, the wind flow along the field lines anchored below 30° latitude and opened by the plasma outflow at the top of the streamer tends to get attenuated in the absence of wave energy supply and the related open field lines tend to become closed via magnetic reconnection. The second factor is the magnetic configuration within the streamer which is determined mainly by the latitudinal span of the streamer base and the magnitude of the magnetic flux in the streamer. The larger the latitudinal span and the magnetic flux are, the higher the streamer top will be in the corona, and the more field lines in the outermost part of the streamer will be opened by the hot plasma. This conclusion was confirmed by simulations where the streamer base border is fixed at 30° latitude but the magnetic flux is varied. When this flux is twice that emerging from the coronal base above 30° latitude, for instance, the outermost part (to be exact, about 0.5%) of the flux became open, leading to a mixture of open and closed field lines. The larger the magnetic flux is, the more flux will become open. However, when the magnetic flux is moderate, say, being the same as that above 30° latitude, as specified in this study, the field lines emerging below 30° latitude turn out to be almost completely closed as obtained by the numerical results. This indicates that our model allows the field lines to be freely opened by the hot plasma without taking any ad hoc measures to maintain the connectivity of these field lines and that the field lines anchored at the streamer base remain closed if the magnetic flux is not too large. Consequently, the border of the non-vanishing wave energy flux (at 30° latitude) naturally forms the boundary between the open and closed fluxes for the present case, and thus the ratio of open to closed flux approximately equals the ratio of the flux below 30° latitude to that above, as previously concluded. Nevertheless, perturbations occur near the border of the streamer and near the equatorial current sheet due to the plasma outflow from the top of the streamer and the magnetic reconnection across the current sheet, which hinders numerical solutions from approaching a quasi-steady state. In contrast with the solution presented by *Washimi et al.* [1987], the perturbations in our case cause only an oscillation of the numerical solution around a steady state without any systematic deviations. All the statements made above were demonstrated by our numerical simulations. Incidentally, the perturbations may be reduced by a special measure similar to that used by *Hu et al.* [2003] without significant effect on the resultant quasi-steady state, and we will address this issue in section 3.2. Figure 2b shows the final magnetic configuration obtained for specific case A (see section 4), that has the required flux distribution on the solar surface.

[22] Given the boundary conditions at the coronal base, the time-dependent solution converges eventually to a unique steady state, as demonstrated by the numerical examples in section 4. Consequently, the initial conditions may be specified arbitrarily in various ways. For instance, we may take the following initial conditions: (1) v_r increases monotonically from 1 km·s^{-1} at the coronal base to 500 km·s^{-1} at the top for the inner subdomain, whereas it is constant along the r-direction for the outer subdomain, equal to that at the lower boundary. The initial value of v_θ is set to be zero everywhere in both subdomains. (2) The other quantities decrease monotonically with r according to $r^{-2/7}$ for T_e and T_p, r^{-3} for ρ, and $r^{-3.5}$ for p_w. Actually, we may even take the initial radial velocity to be zero or take a uniform temperature along the radial direction, the numerical solution reaches the same steady state that does not depend on the initial conditions, as expected.

3. Numerical Method and Techniques

[23] The multistep implicit scheme [*Hu*, 1989] is used to solve equations (2)–(7). This scheme has an excellent stability for long-term calculation and is stable for β values as small as 10^{-4}. Besides, due to the implicit treatment, the

scheme generally allows a much larger time step than that required by the conventional CFL condition [*Richtmyer and Morton*, 1967]. This makes the scheme very efficient. However, when used for steady solar wind problems, certain refinements of the original version of the scheme must be made, and they will be described below.

3.1. Numerical Dissipation and Stability

[24] The original version of the multistep implicit scheme included the Lapidus artificial dissipation to maintain numerical stability with the dissipation coefficient proportional to the magnitude of flow velocity gradient [*Lapidus*, 1967; *Hu*, 1989]. While applied to magnetostatic equilibrium problems, such artificial dissipation will not affect the numerical results because it disappears everywhere in the numerical box when the flow velocity approaches zero. For strong disturbances in a static atmosphere, this dissipation will not bring about a serious distortion of the simulation results, since it is limited to the disturbed region with large velocity gradients. However, for steady solar wind problems, plasma flow is ubiquitous, and thus the Lapidus artificial dissipation will take energy away from the system in vain. We tested the original version of the multistep implicit code with Lapidus artificial dissipation (that was used successfully to simulate catastrophic behaviors of magnetostatic equilibria in the solar atmosphere [e.g., *Hu and Liu*, 2000; *Hu*, 2001, *Hu and Jiang*, 2001; *Hu et al.*, 2001, 2003]) for 2-D solar wind problems and found that the energy of the system was far from being conserved: one had to provide more energy to the solar wind than that required, and a significant part of the supplied energy was dissipated away by the artificial dissipation. Therefore we will seek an alternative way to the Lapidus dissipation method to stabilize the code without producing any significant dissipation. It was found that numerical instabilities of the multistep implicit scheme were closely related to the so-called "checker board" errors inherent to the central difference adopted in this scheme [see *Hu*, 1989]. Tentative operation of the code indicated that the calculation may proceed stably if one can efficiently suppress the "checker board" errors. The following measure is taken to remove these errors. Suppose that a solution along either the radial or the colatitudinal direction is denoted by $\{u_1, u_2, \ldots, u_N\}$, and it has "checker board" errors. Now let us add a positive dissipation to u_j by

$$u_j^d = u_j + 0.25\left(u_{j+1} + u_{j-1} - 2u_j\right), \quad (j = 2, 3, \ldots, N-1),$$
$$u_1^d = u_1, \qquad u_N^d = u_N, \tag{21}$$

so as to get u_j^d, that will have no "checker board" errors. Then a negative dissipation is exerted on u_j^d in terms of

$$u'_j = u_j^d - f_j + f_{j-1}, \quad (j = 2, 3, \ldots, N-1),$$
$$u'_1 = u_1, \qquad u'_N = u_N, \tag{22}$$

where

$$f_j = s_j \max\left\{0, \min\left(s_{j-1}\Delta u_{j-1}^d, 0.25\left|\Delta u_j^d\right|, s_{j+1}\Delta u_{j+1}^d\right)\right\},$$
$$\Delta u_j^d = u_{j+1}^d - u_j^d, \qquad s_j = \mathrm{sign}\left(1,\ \Delta u_j^d\right).$$

Here u'_j is taken as the updated solution instead of u_j. As a result, in flow regions without "checker board" errors the positive dissipation exerted on the solution by equation (21) is almost corrected by the antidissipation of equation (22), whereas the "checker board" errors disappear from other regions. This procedure is the same as the FCT (flux-corrected transport) method [*Boris and Book*, 1973, 1976; *Book et al.*, 1975]. The correction made by equation (22) is not thorough, of course, so slight dissipation is still added to the solution by the operations of equations (21) and (22). Fortunately, we do not have to execute the operations every time step in order to suppress the "checker board" errors and stabilize the code. Instead, we may execute equations (21) and (22) every 20 or more time steps, provided the code works stably. By the way, these operations will not be made on ψ in order to avoid additional numerical diffusion of the magnetic field. The code thus obtained works stably with negligible numerical dissipations, and the relevant conservation laws are well satisfied by the numerical solution. We will give a quantitative analysis of this issue in section 4.

3.2. Reduction of Numerical Oscillations in the Solutions

[25] As mentioned in section 2.3, the plasma outflow from the top of the streamer and the numerical reconnection across the equatorial current sheet cause oscillations of the numerical solution around a steady state. For instance, the magnetic flux function ψ oscillates around ψ_c along the equatorial current sheet. Note that $\psi = \psi_c$ serves as the boundary between the streamer and the solar wind region, and ψ is larger than ψ_c on the streamer side. When ψ at the current sheet becomes smaller than ψ_c, a part of the field lines anchored in the quiet Sun region right next to the streamer becomes closed and joins the streamer. However, these newly closed field lines will be soon forced to reopen by the Alfvén waves emanating from their footpoints at the coronal base. Numerical simulations showed that such a closing-reopening process of the field lines located in the solar wind region made a major contribution to the oscillation of the solution. To prevent such a contribution, we simply set a lower limit, ψ_c, on the updated ψ along the equatorial plane at each time step. By doing so, numerical reconnection of the field lines in the solar wind region is prohibited, and the oscillation of the numerical solution in the neighborhood of the current sheet is substantially reduced. This makes the solution more stable and accurate in the slow wind region. Nevertheless, it should be emphasized that even if no limitation is imposed on the magnetic flux function at the equatorial current sheet, the quasi-steady state solutions obtained are almost the same as those presented in this paper, except that slightly larger oscillations appear in the solar wind region. We point out in passing that ψ is still allowed to exceed ψ_c along the equatorial current sheet. This implies that the closed flux in the outer part of the streamer where $\psi > \psi_c$ is allowed to be opened up presumably by the plasma outflow from the top of the streamer. The newly opened flux turns closed through magnetic reconnection, leading to the formation of outward moving blobs along the equator. This is the main cause for the remnant oscillation of the numerical solution especially near the equatorial plane, as will be shown in

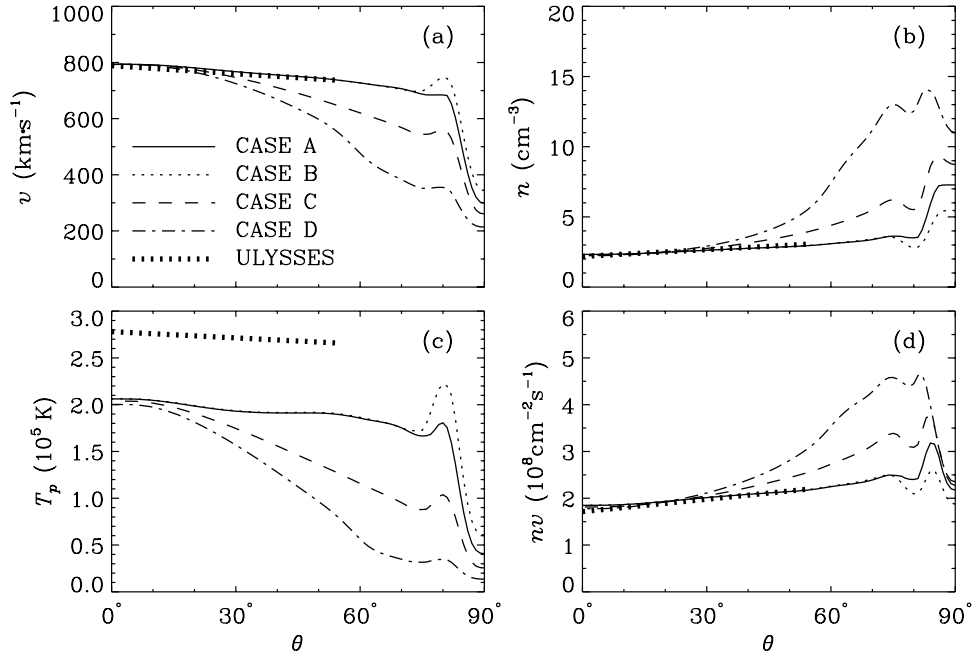

Figure 3. Comparison of the profiles at 1 AU of (a) velocity, (b) density, (c) proton temperature, and (d) mass flux, for cases A, B, C, and D, as a function of colatitude ($\theta = 0°$ at the pole), with those measured by Ulysses (thick dots).

section 4.3. Such blobs were observed by SOHO/LASCO but are believed not to affect the quasi-steady state of the helmet streamer [*Wang et al.*, 1998]. To simulate these blobs, we had better to use resistive MHD model and to further raise the spatial resolution of the code, and this is beyond the scope of this study.

3.3. Time Step Length

[26] For an explicit scheme, the time step length is subject to the constraint of the well-known Courant-Friedrichs-Lewy (CFL) condition [*Richtmyer and Morton*, 1967]; namely, within each time step, the distance through which a signal travels should be less than the smallest spacing of the mesh multiplied by the so-called CFL number that is $\sqrt{2}/2$ for 2-D cases. For the present multistep implicit scheme, the CFL number may be taken larger than unity if the solution is not very far from a steady state. Generally speaking, the closer the solution comes to a steady state, the larger the allowed CFL number will be for stable calculations. Through numerical tests we found the following heuristic expression for the time step length:

$$\Delta t = \max\left\{C_1 \min_{i,j}\left(\frac{dr_i}{v_{ri,j}+v_{fri,j}}, \frac{r_i d\theta_j}{v_{\theta i,j}+v_{f\theta i,j}}\right), \quad C_2 \min_k\left(\frac{1}{|W_k|}\right)\right\}, \tag{23}$$

where v_{fr} and $v_{f\theta}$ are the fast wave speed along the r- and θ-directions, C_1 is the CFL number, C_2 is another constant, subscripts i and j go through all grid points, and subscript k labels the seven dependent variables. Each of W_k represents the left-hand side of the related time-dependent equation as given by equations (2)–(7), exclusive of the temporal derivatives. Equation (23) serves as a useful criterion for the time step determination. When a state comes close to a steady one during the time evolution, W_k ($k = 1,\ldots,7$) becomes small, Δt is actually determined by the second term in the parentheses of equation (23), and thus the effective CFL number may be much larger than C_1. This rendered the code very efficient. C_1 and C_2 are determined by tentative calculations. We take $C_1 = 0.2$ for both subdomains and $C_2 = 0.05$ for the domain of (1–10 R_s) and 0.01 for the domain of (10–215 R_s). The effective CFL number may reach 2 to 3 when the solution approaches a steady state.

4. Numerical Results

[27] As previously mentioned, we have selected four cases, labeled A, B, C, and D, respectively, based on different choices of the distribution of the wave dissipation length L_{c0}. A brief comparison will be made between these cases, while detailed discussions will focus on case A with emphasis on the origin of the fast and slow wind.

4.1. Comparison Between the Four Cases

[28] The steady state solutions for cases A, B, C, and D, and the resultant colatitudinal profiles at 1 AU, are shown in Figure 3 for the flow velocity v ($=(v_r^2 + v_\theta^2)^{1/2}$), number density n ($= \rho/m_p$), proton temperature T_p, and proton flux nv, respectively. For comparison, the corresponding Ulysses observations are also shown by thick dotted curves, which are the linear fits of the Ulysses data given by *McComas et al.* [1998] in the range of colatitude between 0° and 54°. Notice that the linear fit for the total mass flux at 1 AU was reduced by 17% in order to subtract the contribution made by alpha particles with an abundance of 4.3%. The profiles for case A (solid line) match the Ulysses measurements very well except for the profile of T_p that has nearly the same slope but is below the observed profile

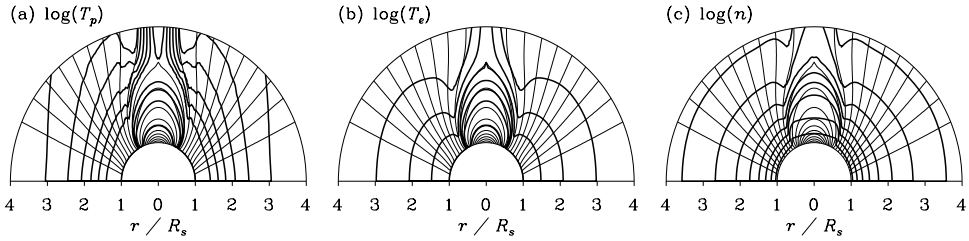

Figure 4. Contours of proton temperature T_p, electron temperature T_e, and number density n for case A. The contour levels are equally spaced by 0.1 for log T_e and log T_p (K) and 0.5 for log n (cm^{-3}), with the first level being 6 for log T_e and log T_p and 8 for log n.

by about 0.6×10^5 K. We tried to raise the predicted profile of T_p by adjusting the wave amplitude and dissipation length while maintaining the profiles of other quantities essentially unchanged but did not succeed. It implies that the model falls short in providing the necessary extended heating. As pointed out by some previous 1-D Alfvén-wave-driven solar wind models [*Hollweg and Johnson*, 1988; *Isenberg*, 1990; *Hu et al.*, 1999], this problem stems from the specific spatial distribution of the heat deposition given by equation (14). There might be certain ways to solve it, say, by using Tu's cascade model [*Tu*, 1987; *Hu et al.*, 1999], by including the proton thermal conduction [*Li et al.*, 1999], or simply by adding an r-dependent dissipation length for the waves [*Usmanov et al.*, 2000]. They are worth trying to further refine the present 2-D model but are beyond the scope of this study.

[29] The solution for case B is close to that for case A except that an overshoot appears in the profiles of v and T_p around $\theta = 10°$, and a corresponding undershoot appears in the profiles of n and nv. The reason lies in that the dissipation length L_{c0} for case B is too large for flow tubes near the equator ($0.8\psi_c \leq \psi < \psi_c$, see Figure 1d). By a proper reduction of L_{c0}, we return to case A, for which such overshoots and undershoots almost disappear. As far as the other two cases are concerned, either the increase of L_{c0} with colatitude is too slow or L_{c0} is uniform everywhere on the solar surface so that v and T_p drop and n and nv grow with colatitude more rapidly than those observed.

[30] At present, it is physically unclear why Alfvén waves should have a dissipation length L_{c0} on the solar surface like that described by equation (18). Nevertheless, it is not very meaningful to explore the physical reason, since the Kolmogorov dissipation rate has limitations as mentioned above on one hand, and there certainly exist exotic energy sources other than Alfvén waves for the solar wind on the other. We would not rely on a strange specification of L_{c0} to match the numerical solution with Ulysses observations, if other dissipation mechanisms for the waves or other driving sources were adopted.

4.2. Properties of the Solution for Case A

[31] In what follows, we will focus on case A and give a detailed analysis of the numerical solution.

4.2.1. Helmet Streamer

[32] First of all, let us look at the streamer region. Figure 4 shows the contours of T_p, T_e, and n, in the region of 1–4 R_s as thick solid curves and the field lines as thin solid curves. The field lines are shown in Figure 2b, with the cusp point at about 3 R_s. In the region below 4 R_s, log T_p (K) is in the range of 5.82–6.58, log T_e 5.60–6.30, and log n_e (cm^{-3}) 4.33–8.48. It can be seen that the contours of both T_p and T_e almost completely coincide with the field lines in the streamer region, and the two temperatures are almost equal everywhere in this region. Such a result is not strange and stems from the fact that v and p_w, hence the heating rate Q, vanish in the streamer. As a result, equations (5) and (6) reduce to

$$\nu_E(T_e - T_p) - \frac{\gamma - 1}{\rho R}\nabla \cdot (\mathbf{K}_e \cdot \nabla T_e) = 0, \quad \nu_E(T_p - T_e) = 0, \tag{24}$$

for the steady state, leading to the conclusion that $T_p = T_e$ and $\mathbf{B} \cdot \nabla T_e = 0$, which are well reproduced by the numerical results. Moreover, we have specified a uniform temperature and density distribution at the base of the streamer (see equations (12) and (13) and Figure 1b). As a result, the streamer becomes isothermal except in the boundary layer, where the temperature jumps from 2×10^6 K on the inner side to 10^6 K on the outer side. Along each field line we have from equation (3)

$$\mathbf{B} \cdot \left[\nabla(p_e + p_p) + \frac{\rho G M_s}{r^2}\hat{\mathbf{r}}\right] = 0. \tag{25}$$

Consequently, the density decreases with height in the same manner everywhere within the streamer, so its contours within the streamer are parallel to the solar surface (see Figure 4c). Then the gas pressure gradient has no transverse component, and the Lorentz force vanishes. Therefore the plasma inside the streamer is in isothermal static equilibrium, whereas the magnetic field is potential there. Such a result comes from the choice of a uniform temperature and density at the base of the streamer, of course. As a matter of fact, in the boundary layer of the streamer, where both density and temperature change in the transverse direction, the plasma is in magnetostatic equilibrium and the magnetic field is no longer potential.

[33] The results are not only physically reasonable, but also agree with recent SOHO/UVCS observations [*Li et al.*, 1998]. The predicted density and temperature are 1.5×10^8 cm^{-3} and 2×10^6 at $1.15R_s$, respectively. These numbers are within the range of observed values. Besides, Li et al.'s analysis led to the conclusion that the streamer is close to isothermal, which is in accordance with the model prediction. Incidentally, the T_e contours outside the streamer are nearly parallel to the solar surface, implying that no appreciable electron thermal conductive flux crosses the

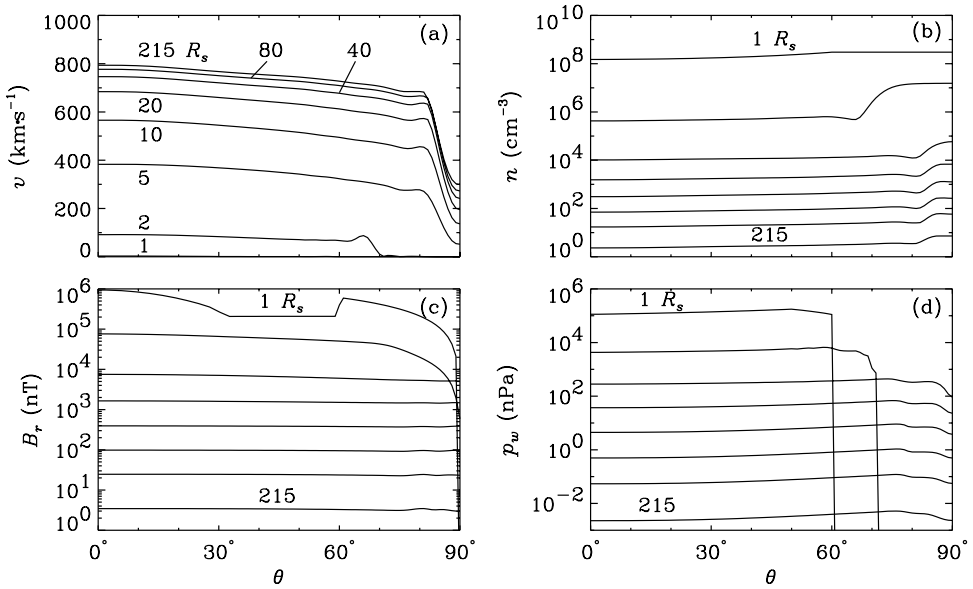

Figure 5. Colatitudinal profiles of (a) velocity, (b) density, (c) radial magnetic field, and (d) wave pressure, for the solution of case A, at heliocentric distances of 1, 2, 5, 10, 20, 40, 80 and 215 R_s.

streamer border in the numerical solution. If an isotropic thermal conductivity were used for electrons, we would have the hot streamer as a heat reservoir that receives heat flux from below the streamer base and launches heat flux to the surrounding open field region. Thus the resultant solar wind would be remarkably different.

4.2.2. Global Properties of the Solar Wind

[34] Figure 5 shows the colatitudinal profiles at several separate heliocentric distances for v, n, B_r, and nv. All profiles are labeled by their respective heliocentric distances in Figure 5a, but only the highest and lowest profiles are labeled in the other panels for conciseness, since the corresponding heliocentric distances change monotonically with the position of the profiles in these panels.

[35] The flow velocity is in the range of 1–3 km·s^{-1} at 1 R_s, too small to be appreciable in Figure 5a. Each v profile has a knee-point, beyond which v drops sharply with colatitude. The colatitude of this point increases with heliocentric distance and reaches an almost constant value of 81° beyond 3.5 R_s. The locus of these knee-points actually constitutes the boundary of the fast solar wind; namely, the fast wind predicted by our model extends from the pole to a latitude of 9°. The wind emerging from the polar coronal hole belongs to the fast one, but it occupies only the part above 30° latitude. Therefore the fast wind at latitudes between 9° and 30° comes from the quiet sun around the polar coronal hole, and it stands for about 40% of the fast wind. This conclusion does not depend on the special choice of the magnetic flux distribution given by equation (11), and the given width of the streamer base but rather, is based on the assumption that the polar coronal hole is responsible for one half of the interplanetary magnetic flux. What we have done is simply to demonstrate that the open field region outside the polar coronal hole can launch fast wind in almost the same way as the coronal hole does. This region is necessary to cover the deficit of the open magnetic flux from polar coronal holes, as already mentioned in both the introduction and section 2.2.1. A definite percentage of the fast solar wind actually coming from the quiet Sun relies on an accurate estimate of the share of the open magnetic flux from this region in the total IMF flux. However, it is our belief that polar coronal holes are certainly not the unique source of the fast solar wind. Incidentally, while the fast wind emerging from the quiet Sun has a slightly lower wind speed than that from the polar coronal hole, it has a larger density and a larger mass flux as well. Besides, its origin is closer to the ecliptic plane, so the fast wind at Earth should mostly come from the quiet Sun instead of the polar coronal hole during solar minimum. At lower latitudes below the knee-points, the wind speed decreases sharply with colatitude. The lowest speed is about 300 km·s^{-1} at 1 AU. Given an upper limit of 400 km·s^{-1}, the slow wind has a half-width of 4°. In the transition region between the slow and fast wind of 5° in width, the wind speed increases from 400 to 700 km·s^{-1}.

[36] As seen from Figure 5b, the density increases monotonically with colatitude at all heliocentric distances, except for a small dip around the knee-point. In particular, in or above the quiet Sun region, the density is higher than that in the polar coronal hole. This is probably the reason why as an open field region on the solar surface and an additional source of the fast wind, the quiet sun was observationally distinguished from polar coronal holes by *Habbal and Woo* [2001].

[37] The radial magnetic field at large distances becomes nearly uniform, varying between 3.0 and 3.5 nT (see Figure 5c), that is essentially consistent with the observational conclusion that r^2B_r does not show any appreciable latitudinal dependence [*Smith and Balogh*, 1995]. Notice that the heliospheric current sheet appears as a tip in the colatitudinal profile of ψ, across which $\partial\psi/\partial\theta$ changes sign. Therefore in our model the current sheet manifests itself as an ideal tangential discontinuity of zero width, across which B_r changes in sign. The profile of B_r is flat in the vicinity of the current sheet, which is also consistent with observations.

[38] The wave pressure is lower in the equatorial plane below 20 R_s, but becomes slightly larger beyond 20 R_s than

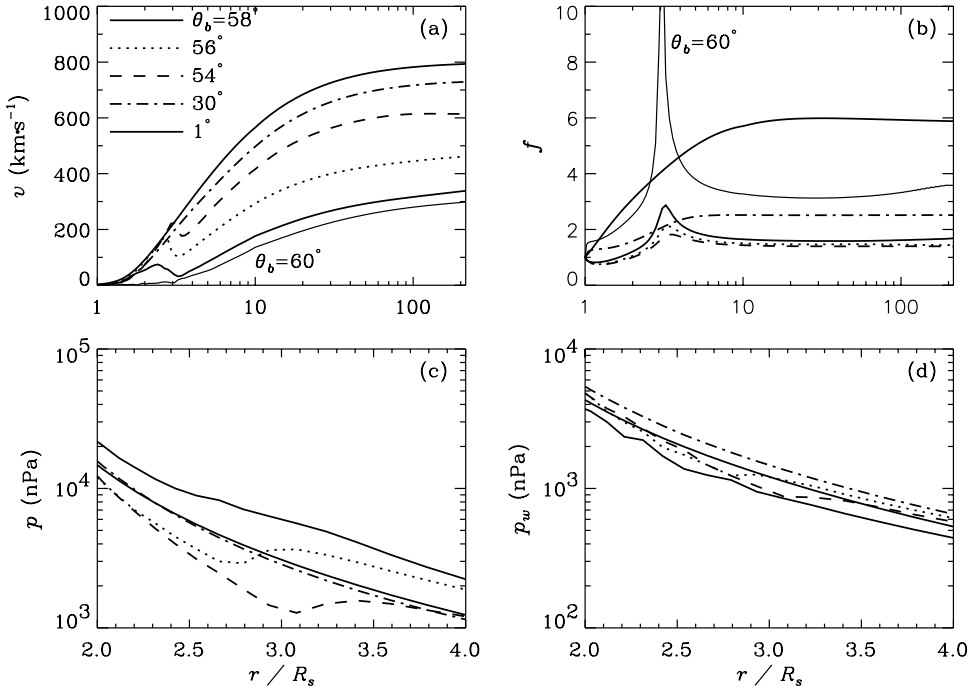

Figure 6. Profiles of (a) velocity v, (b) expansion factor f, (c) gas pressure p, and (d) wave pressure p_w, along different flow tubes anchored on the solar surface at θ_b = 1°, 30°, 54°, 56°, and 58°, respectively. The thin solid curve in Figures 6a and 6b corresponds to the flow tube passing through the cusp point with its footpoint right at the streamer border (θ_b = 60°).

that along the polar axis (Figure 5d). The former is attributed to a lower wave pressure specified on the solar surface in the neighborhood of the streamer (see Figure 1c), whereas the latter stems from a smaller dissipation rate or a larger dissipation length in the same region (see Figure 1d). The existence of Alfvén waves in both fast and slow winds with comparable amplitude is consistent with relevant observations [*Marsch et al.*, 1981; *Roberts et al.*, 1987].

4.2.3. Origin of the Slow Wind

[39] Like most previous 2-D models, a slow wind appears in a narrow belt astride the equatorial plane, as shown in Figure 5a. The existence of such a slow wind belt is mainly attributed to the flow tube geometry rather than the driving mechanism. To the best of our knowledge, *Wang and Sheeley* [1990] were the first to realize the importance of the flow tube geometry for the origin of the slow wind. They found an inverse correlation between the wind speed at 1 AU and the divergence rate of the coronal magnetic field near the Sun and thus suggested that nonmonotonic expansion factors should be included in solar wind models. *Chen and Hu* [2001, 2002] did take the effect of flow tube geometry into account and found that with the same flow conditions and wave properties specified at the coronal base, an expansion factor which increases monotonically with heliocentric distance results in a fast solar wind solution, whereas a flow tube which undergoes an expansion-contraction-reexpansion process creates a slow solar wind solution. Here we obtained similar results, but we hope to find some dynamical reasons. Figure 6a shows the flow velocity v along several separate flow tubes rooted at θ_b = 1°, 30°, 54°, 56°, and 58° on the solar surface. For flow tubes at high latitudes (θ_b = 1° and 30°), v increases monotonically with r, whereas it shows a nonmonotonic variation for flow tubes close to the helmet streamer (θ = 54°, 56° and 58°). The former corresponds to the fast wind, and the latter corresponds to the slow and intermediate wind. The expansion factor f, defined as the ratio between the cross-section area of the flow tube and r^2, is shown in Figure 6b as a function of r for these flow tubes. All flow tubes with slow and intermediate wind speeds have nonmonotonic expansion factors. In particular, the flow tube along the streamer border and equatorial current sheet (θ_b = 60°) has an infinite expansion factor at the cusp point where both v and B vanish. *Strachan et al.* [2002] found that the O^{5+} outflow velocity vanishes near the cusp point and increases gradually along the streamer stalk beyond the cusp. Indeed, the velocity profile for θ_b = 60° in Figure 6a shows a similar behavior. It is interesting to note that the profiles of the gas pressure (Figure 6c) and wave pressure (Figure 6d) are flattened or have a bump near the cusp point along the flow tubes with slow or intermediate wind speeds. This results in a small upward or even a downward pressure gradient force there, leading to the localized deceleration of the solar wind. As a result, the slow wind has a nonmonotonic velocity profile along the flow tube. A rapid expansion followed by a rapid contraction of the solar wind plasma is probably the dynamical cause for the flattened pressure profiles or the ones with a bump, which leads to the formation of the slow wind. Incidentally, similar dips in the flow velocity near the cusp point were found by 1-D models [e.g., *Cuperman et al.*, 1990; *Vasquez et al.*, 1999; *Suess and Nerney*, 2002], but our solution recovers this feature for a special 2-D case.

[40] The behavior of the solution in the slow wind region leads to a special behavior of the sonic curve where the

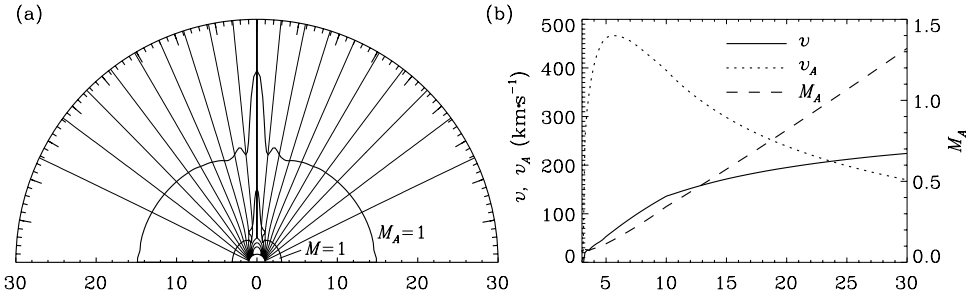

Figure 7. (a) The sonic curve ($M = 1$) and the Alfvén curve ($M_A = 1$) by thick solid lines along with the magnetic configuration by thin solid lines. (b) The radial profile of v, v_A, and M_A along the equator.

flow speed equals the sound speed ($v = a \equiv (\gamma R(T_p + T_e))^{1/2}$ or $M = v/a = 1$) and the Alfvén curve where the flow speed equals the Alfvén speed ($v = v_A \equiv (B/(\mu_0\rho)^{1/2}$ or $M_A = v/v_A = 1$). These curves are shown in Figure 7a along with the field lines. The sonic curve looks like that obtained in previous studies, but a twist appears in the slow wind region. This implies that in some slow wind flow tubes there exist three sonic points where $M = 1$. Obviously, such a new result is closely related to the nonmonotonic velocity profile of the slow wind. As far as the Alfvén curve is concerned, it is critically different from what was obtained in previous studies in the narrow region around the equator. As Figure 7a shows, the Alfvén curve sticks out around the equator, jumping from 15 R_s in the fast wind to 24 R_s at the equator, whereas previous studies [e.g., *Steinolfson et al.*, 1982; *Usmanov et al.*, 2000] predicted an opposite result. The origin of this discrepancy stems from the treatment of the heliospheric equatorial current sheet. In previous studies, the current sheet was spread across the latitudinal direction, forming a transition layer of finite width. For instance, the transition layer obtained by *Usmanov et al.* [2000] has a latitudinal half-width of 10°, spreading over the whole slow wind region (see Figures 5a and 4b in that paper). The Alfvén speed vanishes at the equator and increases in magnitude with latitude. M_A approaches infinity beyond the cusp point at the equator. Consequently, the resultant Alfvén curve dives into the cusp point, forming a deep dimple around the equator. By contrast, we treat the current sheet as an ideal tangential discontinuity, and the profile of the radial magnetic field is flat in the vicinity of the current sheet, as shown in Figure 5c. The Alfvén-Mach number $M_A = \mu_0^{1/2}(\rho v/B)\rho^{-1/2}$ is proportional to the mass flux, via $\rho v/B$, and is inversely proportional to the square root of density. Considering that the mass flux varies much more slowly with latitude than the density, M_A should be smaller in the slow wind than in the fast wind at the same heliocentric distance. As a result, we obtain an Alfvén curve that is projecting around the equator. Within the current sheet the Alfvén curve is indented with a shape similar to that predicted by previous studies, but the width of the current sheet is expected to be very thin. The observed width of the heliospheric current sheet was less than 10^4 km at 1 AU [*Winterhalter et al.*, 1994] that stands for a latitudinal width of only 0.004°. In situ observations are not available for the current sheet width in the inner corona, but we conjecture that this width is of the same order. It seems that for global MHD simulations it is more appropriate to treat the current sheet as a tangential discontinuity than to spread it over the whole slow wind region. Therefore we argue that the Alfvén curve that we obtained in the slow wind region is physically more realistic and reasonable than that obtained by previous models. Figure 7b shows the radial profiles of v, v_A, and M_A along the equator. Near the cusp point ($r \approx 3\ R_s$), both v and v_A approach zero, but M_A is finite. Starting from that point, M_A increases monotonically with r and reaches unity at about 24 R_s. This is consistent with the inverse proportion between M_A and the square root of density along the equator.

4.3. Convergence to Steady State

[41] One of the difficulties with any time-dependent solar wind code is to guarantee that a final steady state has been reached. So far, in existing 2-D simulations, such a convergence has not been definitely established. For example, *Washimi et al.* [1987] give a set of figures showing the temporal variation of the density and flow velocity during the simulation where there is a 1% variation per hour in physical time with no indication that such a variation would stop. They conclude that an exact steady state solution in MHD simulations was a problem for future studies. For 1-D solar wind simulations, however, it has been currently established that if the boundary conditions at the coronal base are properly specified, the time-dependent solution must converge to a steady state that is unique. Hence the same conclusion should hold for multidimensional solar wind simulations, since the solar wind in such simulations consists, in principle, of many thin flow tubes. We show here that we do indeed achieve a unique steady state solution with the 2-D MHD code developed for this study.

[42] The main factor that influences the convergence of time-dependent solar wind solutions is the energy balance in the streamer. If an energy source is applied to the helmet streamer, the streamer has no way of releasing this continual addition of energy but to evolve with time until the field is fully open to the interplanetary medium [*Suess et al.*, 1996]. In the solar wind simulations given here, there is no external energy supply to the streamer since the Alfvén waves, which are the only external energy source, vanish there. The only energy supply, namely, the electron thermal conductive flux across the base of the streamer, eventually stops when the plasma becomes isothermal along each field line in the streamer. The 2-D time-dependent solar wind solutions thus obtained were found to be convergent.

[43] It takes about 200 hours in physical time to reach a steady state in both subdomains, if the initial state is arbitrarily set up. As a rule, the simulation in the inner

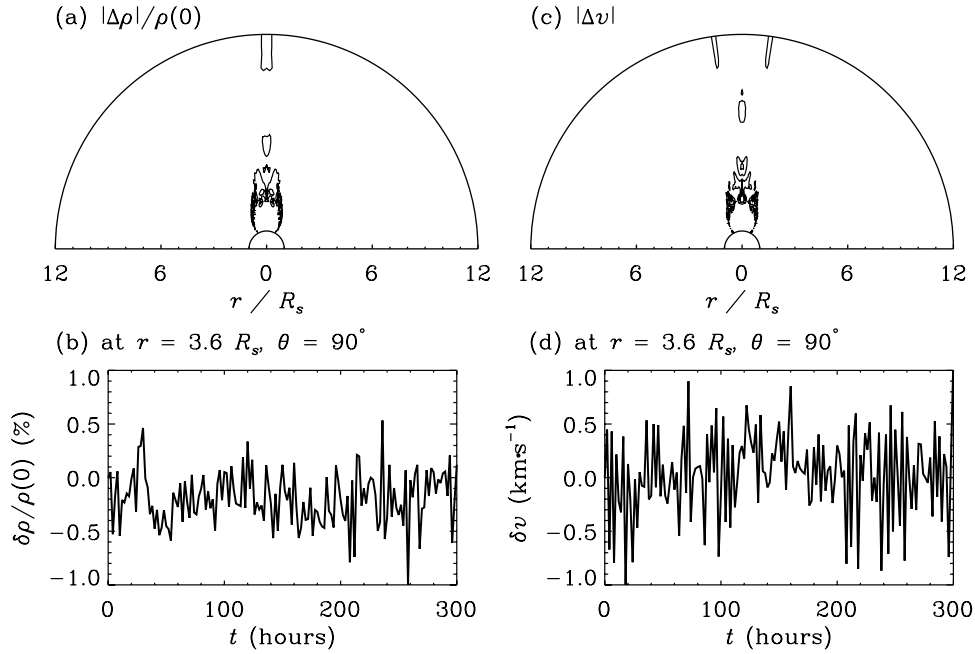

Figure 8. Convergence of the solution with time: The solution of case A was left to evolve with time for a period of 300 hours in order to demonstrate the convergence of the 2-D time-dependent solutions. $\Delta\rho$ and Δv denote the density and flow velocity deviations of the solution at t = 300 h from the solution at t = 0, $\delta\rho$ and δv are the differences between the values at time t and 0 at the grid point $(r, \theta) = (3.6\ R_s, 90°)$ that is right above the cusp point. (a) The contours of $|\Delta\rho|/\rho(0)$ ($\rho(0)$ is the solution of case A at levels 0.5%, 1.0%, and 1.5% (the maximum deviation is 1.99%). (c) Contours of $|\Delta v|$ at levels of 0.5, 1.0, and 1.5 km·$^{-1}$ (the maximum deviation is 1.77 km·s^{-1}). (b) and (d) $\delta\rho/\rho(0)$ and δv as a function of time during the 300-hour period. Notice that the deviation is concentrated in the neighborhood of the streamer border, the cusp point, and the equatorial current sheet. It oscillates around zero in a random way without introducing any systematic shift in the solution from the original steady state.

subdomain is more computer-time consuming. If a steady state solution obtained, say in case A, is taken to be the initial state in this subdomain, then the computer time necessary for getting a steady state solution for another case, B, C, or D, will be substantially reduced, normally by one order of magnitude. To check the convergence, we took the solution of case A as the initial state and continued the simulation in the inner subdomain with the same boundary conditions at the coronal base, including the same dissipation length L_{c0}, for 300 hours in physical time. Then we got the time-dependent solution, sampled every 2 hours till 300 hours. The difference between the initial solution and the newly obtained time-dependent solution is found to be very small. Figure 8a shows the contours of the density difference in percentage between the initial state and the final state at t = 300 hours with three levels: $\Delta\rho/\rho(0)$ = 0.5%, 1.0% and 1.5%, where $\Delta\rho \equiv \rho(300) - \rho(0)$. In the fast wind region, the relative difference is of the order of 10^{-4}–10^{-3}, within the numerical accuracy of the code. In the vicinity of the streamer border, the cusp point, and the equatorial current sheet, the maximum deviation is only 1.99%. Moreover, such deviations oscillate around zero without causing any systematic variation in the solution. Taking the grid point at $(r, \theta) = (3.6\ R_s, 90°)$ as an example, that is above and very close to the cusp point at which the deviation amplitude is the largest, the relative deviation of the time-dependent solution from the initial, $\delta\rho/\rho(0)$ ($\delta\rho \equiv \rho(t) - \rho(0)$), is shown in Figure 8b as a function of time, oscillating around zero in a random manner. As mentioned in section 3.2, this oscillation is associated with the opening of the field lines by the plasma outflow at the top of the streamer and the follow-up closing due to magnetic reconnection. We also show the deviations of the flow velocity in Figures 8c and 8d, where $\Delta v \equiv v(300) - v(0)$ and $\delta v \equiv v(t) - v(0)$. The contour levels are 0.5, 1.0, and 1.5 km·s^{-1}. The maximum deviation is found to be 1.77 km·s^{-1} between the initial state and the final state, and the relatively large deviation is concentrated in the same location as the density deviation does. The velocity deviation is of the order of 0.01–0.1 km·s^{-1} in the fast wind region. Also, the deviation is oscillatory around zero without causing any systematic variation of the solution. The same conclusions hold for other quantities for which the deviations will not be shown here for brevity. Therefore we conclude that the 2-D time-dependent solution does converge to a unique steady state, that depends on the given boundary conditions at the coronal base.

4.4. Conservation Accuracy

[44] The energy conservation law must be satisfied in solar wind simulations, since a major concern of the solar wind study is how the solar wind plasma is heated and accelerated. We also need to check the conservation of mass, but the momentum conservation law is trivially satisfied for axisymmetrical flows. In most 1-D solar wind simulations, various conservation laws were examined and

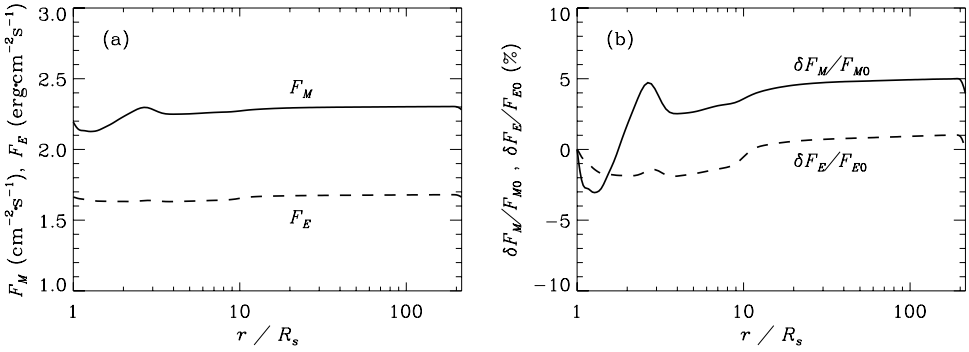

Figure 9. (a) The mean mass flux F_M and (b) the mean energy flux F_E of the solution of case A and their relative deviation from the mean with respect to the corresponding values at the coronal base. The deviation is between −3.1% and 5.0% for F_M and between −1.9% and 1.0% for F_E. By comparing the two fluxes at 1 AU with their counterparts at the coronal base, the deviations turn out to be 3.9% for the mean mass flux and 0.05% for the mean energy flux.

well satisfied. However, similar examination of the conservation laws were ignored in existing 2-D solar wind simulations. We will take care of this issue in our model.

[45] Equation (2) is already in a conservation form for mass, and the conservation form of the energy equation can be derived from equations (2)–(7) as follows:

$$\frac{\partial}{\partial t}\left(\frac{1}{2}\rho v^2 - \frac{\rho G M_s}{r} + \frac{p_e + p_p}{\gamma - 1} + \frac{B^2}{2\mu_0} + 2p_w\right) + \nabla \cdot \left[\left(\frac{1}{2}\rho v^2 - \frac{\rho G M_s}{r}\right)\mathbf{v} + (3\mathbf{v} + 2\mathbf{v}_A)p_w + \frac{\gamma(p_e + p_p)}{\gamma - 1}\mathbf{v} - \mathbf{K}_e \cdot \nabla T_e\right] = 0. \quad (26)$$

The mass and energy conservation laws can be obtained by integrating equations (2) and (26) over a domain between the coronal base and a sphere of radius r with $\partial/\partial t = 0$, respectively. The total mass flux and the total energy flux across the northern hemisphere of radius r, given by

$$\int_0^{2\pi} d\varphi \int_0^{\pi/2} \rho v_r r^2 \sin\theta d\theta = 2\pi R_E^2 F_M(r), \quad (27)$$

and

$$\int_0^{2\pi} d\varphi \int_0^{\pi/2} \left[\frac{1}{2}\rho v^2 v_r + \rho G M_s\left(\frac{1}{R_s} - \frac{1}{r}\right)v_r + \frac{\gamma(p_e + p_p)}{\gamma - 1}v_r + (3v_r + 2v_{Ar})p_w - \kappa_0 T_e^{5/2}\left(\frac{B_r^2}{B^2}\frac{\partial T_e}{\partial r} + \frac{B_r B_\theta}{rB^2}\frac{\partial T_e}{\partial \theta}\right)\right] r^2 \sin\theta d\theta = 2\pi R_E^2 F_E(r), \quad (28)$$

must be equal to their counterparts across the coronal base; namely, both $F_M(r)$ and $F_E(r)$ should be constant, independent of r. The terms in the square parentheses of equation (28) correspond to the fluxes of kinetic energy, potential energy associated with gravity, entropy, wave energy, and electron thermal conduction, respectively. The gravitational potential energy has been set to zero at the coronal base. The total area of the northern hemisphere at $R_E = 1$ AU, $2\pi R_E^2$, has been placed on the right hand side of equations (27) and (28) as a multiplier so that F_M and F_E stand for the mean mass flux and the mean energy flux normalized to 1 AU, respectively. Owing to numerical errors and dissipations, F_M and F_E may not be constant for a solution which is supposed to reach a steady state. We may use them to check the extent to which the two conservation laws are satisfied in the numerical solutions. Figure 9 shows F_M and F_E as a function of heliocentric distance and their relative deviations with respect to the values at the coronal base for the solution of case A. The deviation ranges from −3.1% to 5.0% for the mean mass flux and from −1.9% to 1.0% for the mean energy flux, mainly attributed to numerical errors in the vicinity of the streamer border and the cusp point. If the two fluxes at 1 AU are compared with their counterparts at the coronal base, then the relative deviations amount to 3.9% for the mass flux and 0.05% for the energy flux. Table 1 lists the relevant mean energy fluxes at the coronal base and the Earth orbit, with almost identical total energy flux at the two sites. It can be seen from Table 1 that Alfvén waves provide about 89% of the total energy budget, and the rest comes mainly from the entropy flux and the electron thermal conductive flux. In summary, despite the fact that the solutions obtained were based on a rather coarse difference mesh, the accuracy of the global conservation of mass and energy is basically acceptable.

5. Concluding Remarks

[46] We have improved the multistep implicit scheme, originally developed by *Hu* [1989], for solving axisymmetrical steady solar wind problems in spherical coordinates. It is assumed that Alfvén waves are as the only external source

Table 1. Mean Energy Flux Normalized to 1 AU[a]

Energy Flux	Coronal Base	Earth Orbit
Kinetic energy	4.51×10^{-6}	0.9158
Potential energy	0	0.7212
Entropy	0.1512	0.0169
Wave energy	1.4857	0.0077
Heat conduction	0.0260	5.29×10^{-4}
Total	1.6629	1.6622

[a]Measured in ergs cm^{-2} s^{-1}.

to heat and accelerate the solar wind plasma, and the interplanetary magnetic flux emerges from both the polar coronal hole and the quiet Sun. Through careful selection of the wave energy flux and dissipation length distribution at the coronal base, we found a steady state solution that matches relevant observations quite well. Our main conclusions are summarized as follows:

[47] 1. For conditions typical of solar minimum, by assuming that only half of the interplanetary magnetic flux comes from the polar coronal hole, about 40% of the fast wind is found to originate from the quiet Sun, defined in this study as the open field region surrounding the polar coronal hole. While the actual percentage of the fast solar wind coming from the quiet Sun relies on an accurate estimate of how much of the interplanetary flux originates from polar coronal holes and how much of the heliosphere is filled by the fast wind, it is clear that polar coronal holes are not necessarily the only source of the fast solar wind.

[48] 2. When the open field lines are very close to the helmet streamer, say, within an angular distance of about 6 degrees, the associated flow tubes have a nonmonotonic expansion factor. Such a geometry will lead to a flattened or bumped profile of pressure near the cusp point, and thus a localized deceleration of the solar wind. This is probably the dynamic cause for the formation of the slow wind and the intermediate wind as well. Due to the nonmonotonicity of the flow velocity, a twist appears in the sonic curve in the slow wind region, implying that there exist three sonic points in part of flow tubes in this region.

[49] 3. For the time-dependent solution to converge to a quasi-steady state, one must maintain an energy balance in the streamer. In this study, Alfvén waves are taken to be the only external energy source, propagating strictly along the field lines. Setting the wave energy flux to be zero at the streamer base automatically excludes the wave energy from entering the streamer. On the other hand, the thermal conductive flux across the streamer base vanishes when the plasma becomes isothermal along each field line anchored at the streamer base. The time-dependent solution thus obtained is shown to be convergent to a quasi-steady state that does not depend on the initial guess.

[50] 4. The numerical code for the steady solar wind problem must be low-dissipative in order to achieve a good accuracy of mass and energy conservation. Moreover, in terms of the magnetic flux function ψ, the heliospheric current sheet can be treated as an ideal tangential discontinuity without being spread over a wide transition layer. This substantially raises the numerical accuracy of the magnetic field and flow conditions in the slow wind astride the current sheet. Finally, the numerical reconnection of the open field lines anchored in the quiet sun region right next to the streamer is prohibited simply by setting a lower limit on ψ at the equator. Such a measure may reduce the amplitude of oscillations of the numerical solution especially in the slow wind region without changing the overall final solution in any significant manner.

[51] **Acknowledgments.** This work was supported by NASA grant NAGW-249 of USA, PPARC grant to the University of Wales in Aberystwyth, UK, and grants NNSFC 40274049 and NKBRSF G2000078404 of China. We are grateful to B. Li for useful discussions.

[52] Arthur Richmond thanks Arcadi V. Usmanov, Y.-M. Wang, and another reviewer for their assistance in evaluating this paper.

References

Book, D. L., J. P. Boris, and K. Hain, Flux-corrected transport, 2. Generalizations of the method, *J. Comput. Phys.*, *18*, 248–283, 1975.

Boris, J. P., and D. L. Book, Flux-corrected transport, 1. SHASTA, A fluid transport algorithm that works, *J. Comput. Phys.*, *11*, 38–69, 1973.

Boris, J. P., and D. L. Book, Flux-corrected transport, 3. Minimum-error FCT algorithms, *J. Comput. Phys.*, *20*, 397–431, 1976.

Braginskii, S. I., Transport phenomena in a plasma, in *Reviews of Plasma Physics*, vol. 1, p. 205, Consult. Bur., New York, 1965.

Burlaga, L. F., et al., Sources of magnetic fields in recurrent interplanetary streams, *J. Geophys. Res.*, *83*, 4177–4185, 1978.

Chen, Y., and Y. Q. Hu, A two-dimensional Alfvén-wave-driven solar wind model, *Solar Phys.*, *199*, 371–384, 2001.

Chen, Y., and Y. Q. Hu, Effect of flow-tube geometry on solar wind properties, *Astrophys. Space Sci.*, *282*, 447–460, 2002.

Cuperman, S., L. Ofman, and M. Dryer, Thermally conductive, magnetohydrodynamic flows in helmet-streamer coronal structures, *Astrophys. J.*, *350*, 846–855, 1990.

Geiss, T., et al., The southern high-speed streams: Results from the SWICS instrument on Ulysses, *Science*, *268*, 1033–1036, 1995.

Gosling, J. T., et al., The band of solar wind variability at low heliographic latitudes near solar activity minimum: Plasma results from the Ulysses rapid latitude scan, *Geophys. Res. Lett.*, *22*, 3329–3332, 1995.

Habbal, S. R., and R. Woo, Connecting the sun and the solar wind: Comparison of the latitudinal profiles of coronal and Ulysses measurements of the fast wind, *Astrophys. J.*, *549*, L253–L256, 2001.

Habbal, S. R., et al., Origins of the slow and the ubiquitous fast solar wind, *Astrophys. J.*, *489*, L103–L106, 1997.

Hollweg, J. V., Transition region, corona, and solar wind in coronal holes, *J. Geophys. Res.*, *91*, 4111–4125, 1986.

Hollweg, J. V., and W. Johnson, Transition region, corona, and solar wind in coronal holes: Some two-fluid models, *J. Geophys. Res.*, *93*, 9547–9554, 1988.

Hu, Y. Q., A multistep implicit scheme for time-dependent, two-dimensional magnetohydrodynamic flows, *J. Comput. Phys.*, *84*, 441–460, 1989.

Hu, Y. Q., Catastrophe of coronal magnetic flux ropes in partially open magnetic fields, *Solar Phys.*, *200*, 115–126, 2001.

Hu, Y. Q., and Y. W. Jiang, Catastrophe of coronal magnetic flux ropes caused by photospheric motions, *Solar Phys.*, *203*, 309–319, 2001.

Hu, Y. Q., and W. Liu, A 2.5-D ideal MHD model for coronal magnetic flux ropes, *Astrophys. J.*, *540*, 1119–1125, 2000.

Hu, Y. Q., R. Esser, and S. R. Habbal, A fast solar wind model with anisotropic proton temperature, *J. Geophys. Res.*, *102*, 14,661–14,676, 1997.

Hu, Y. Q., S. R. Habbal, and X. Li, On the cascade processes of Alfvén waves in the fast solar wind, *J. Geophys. Res.*, *104*, 24,819–24,834, 1999.

Hu, Y. Q., Y. W. Jiang, and W. Liu, Coronal magnetic flux rope equilibria and magnetic helicity, *Chin. J. Astron. Astrophys.*, *1*, 77–84, 2001.

Hu, Y. Q., G. Q. Li, and X. Y. Xing, Equilibrium and catastrophe of coronal flux ropes, *J. Geophys. Res.*, *108*(A2), 1072, doi:10.1029/2002JA009419, 2003.

Isenberg, P. A., Investigations of a turbulence-driven solar wind model, *J. Geophys. Res.*, *95*, 6437–6442, 1990.

Krieger, A. S., A. F. Timothy, and E. C. Roelof, A coronal hole and its identification as the source of a high velocity solar wind stream, *Solar Phys.*, *29*, 505–525, 1973.

Lapidus, A., A detached shock calculation by second-order finite differences, *J. Comput. Phys.*, *2*, 154–177, 1967.

Li, J., et al., Physical structure of a coronal streamer in the closed-field region as observed from UVCS/SOHO and SXT/YOHKOH, *Astrophys. J.*, *506*, 431–438, 1998.

Li, X., S. R. Habbal, J. V. Hollweg, and R. Esser, Heating and cooling of protons by turbulence-driven ion cyclotron waves in the fast solar wind, *J. Geophys. Res.*, *104*, 2521–2535, 1999.

Low, B. C., Models of partially open magnetospheres with and without magnetodisks, *Astrophys. J.*, *310*, 953–965, 1986.

Marsch, E., and C.-Y. Tu, Solar wind and chromospheric network, *Solar Phys.*, *176*, 87–106, 1997.

Marsch, E., K.-H. Muhlhauser, H. Rosenbauer, R. Schwenn, and K. U. Denskat, Pronounced proton core anisotropy, ion differential speed, and simulataneous Alfvén wave activity in slow solar wind at 0.3 AU, *J. Geophys. Res.*, *86*, 9199–9203, 1981.

McComas, D. J., et al., Ulysses' return to the slow solar wind, *Geophys. Res. Lett.*, *25*, 1–4, 1998.

McComas, D. J., et al., Solar wind observations over Ulysses' first full polar orbit, *J. Geophys. Res.*, *105*, 10,419–10,433, 2000.

Richtmyer, R. D., and K. W. Morton, *Difference Methods for Initial Value Problems*, Wiley-Interscience, Hoboken, N. J., 1967.

Roberts, D. A., M. L. Goldstein, L. W. Klein, and W. H. Matthaeus, Origin and evolution of fluctuations in the solar wind: Helios observations and Helios-Yoyager comparisons, *J. Geophys. Res.*, *92*, 12,023–12,035, 1987.

Smith, E. J., and A. Balogh, Ulysses observations of the radial magnetic field, *Geophys. Res. Lett.*, *22*, 3317–3320, 1995.

Spitzer, L., Jr., *Physics of Fully Ionized Gases*, Wiley-Interscience, Hoboken, N. J., 1962.

Steinolfson, R. S., S. T. Suess, and S. T. Wu, The steady global corona, *Astrophys. J.*, *255*, 730–742, 1982.

Strachan, L., R. Suleiman, A. V. Panasyuk, D. A. Biesecker, and J. L. Kohl, Empirical densities, kinetic temperatures, and outflow velocities in the equatorial streamer belt at solar minimum, *Astrophys. J.*, *571*, 1008–1014, 2002.

Suess, S. T., and S. Nerney, Stagnation flow in streamer boundaries, *Astrophys. J.*, *565*, 1275–1288, 2002.

Suess, S. T., A.-H. Wang, and S. T. Wu, Volumetric heating in coronal steamers, *J. Geophys. Res.*, *101*, 19,957–19,966, 1996.

Suess, S. T., A.-H. Wang, S. T. Wu, G. Poletto, and D. J. McComas, A two-fluid, MHD coronal model, *J. Geophys. Res.*, *104*, 4697–4708, 1999.

Svalgaard, L., T. L. Duvall, and P. H. Scherrer, The strength of the Sun's polar fields, *Solar Phys.*, *58*, 225–240, 1978.

Tu, C.-Y., A solar wind model with the power spectrum of Alfvénic fluctuations, *Solar. Phys.*, *109*, 149–186, 1987.

Tu, C.-Y., and E. Marsch, Two-fluid model for heating of the solar corona and acceleration of the solar wind by high-frequency Alfvén waves, *Solar Phys.*, *171*, 363–391, 1997.

Ulrich, R. K., Analysis of magnetic flux tubes on the solar surface from observations at Mt. Wilson of λ5250 and λ5233, in *Cool Stars, Stellar Systems, and the Sun*, edited by M. S. Giampapa and J. A. Bookbinder, p. 265, Astron. Soc. of the Pac., San Francisco, Calif., 1992.

Usmanov, A. V., M. L. Goldstein, B. P. Besser, and J. M. Fritzer, A global MHD solar wind model with WKB Alfvén waves: Comparison with Ulysses data, *J. Geophys. Res.*, *105*, 12,675–12,695, 2000.

Vasquez, A. M., A. A. van Ballegooijen, and J. C. Raymond, Model of solar wind flow near an equatorial coronal streamer, in *Solar Wind Nine*, edited by S. R. Habbal et al., *AIP Conf. Proc.*, *471*, 243–246, 1999.

Wang, Y. M., and N. R. Sheeley Jr., The solar origin of long-term variations of the interplanetary magnetic field strength, *J. Geophys. Res.*, *93*, 11,227–11,236, 1988.

Wang, Y. M., and N. R. Sheeley Jr., Solar wind speed and coronal flux-tube expansion, *Astrophys. J.*, *355*, 726–732, 1990.

Wang, Y.-M., and N. R. Sheeley Jr., Solar implications of Ulysses interplanetary field measurements, *Astrophys. J.*, *447*, L143–L146, 1995.

Wang, Y.-M., and N. R. Sheeley Jr., Sunspot activity and the long-term variation of the Sun's open magnetic flux, *J. Geophys. Res.*, *107*(A10), 1302, doi:10.1029/2001JA000500, 2002.

Wang, Y.-M., et al., Origin of streamer material in the outer corona, *Astrophys. J.*, *498*, L165–L168, 1998.

Wang, Y.-M., J. Lean, and N. R. Sheeley Jr., The long-term variation of the Sun's open magnetic flux, *Geophys. Res. Lett.*, *27*, 505–508, 2000.

Washimi, H., Y. Yoshino, and T. Ogino, Two-dimensional structure of the solar wind near the Sun, *Geophys. Res. Lett.*, *14*, 487–490, 1987.

Winterhalter, E., E. J. Smith, M. E. Burton, and N. Murphy, The heliospheric plasma sheet, *J. Geophys. Res.*, *99*, 6667–6680, 1994.

Woo, R., and S. R. Habbal, Extension of coronal structure into interplanetary space, *Geophy. Res. Lett.*, *24*, 1159–1162, 1997.

Woo, R., and S. R. Habbal, Radial evolution of density structure in the solar corona, *Geophy. Res. Lett.*, *12*, 1793–1796, 1999a.

Woo, R., and S. R. Habbal, Imprint of the sun on the solar wind, *Astrophys. J.*, *510*, L69–L72, 1999b.

Woo, R., S. R. Habbal, R. A. Howard, and C. M. Korendyke, Extension of the polar coronal hole boundary into interplanetary space, *Astrophys. J.*, *513*, 961–968, 1999.

Zhao, X., and J. T. Hoeksema, Prediction of the interplanetary magnetic field strength, *J. Geophys. Res.*, *100*, 19–33, 1995.

Zirker, J. B., (Ed.), *Coronal Holes and High Speed Wind Streams*, Colo. Assoc. Univ. Press, Boulder, Colo., 1977.

Y. Chen, Harvard-Smithsonian Center for Astrophysics, Cambridge, MA 02138, USA. (yachen@cfa.harvard.edu)

S. R. Habbal, Y. Q. Hu, and X. Li, Institute of Mathematical and Physical Sciences, University of Wales, Aberystwyth, SY23 3BZ, UK. (sdh@aber.ac.uk; huyq@ustc.edu.cn; xxl@aber.ac.uk)